Nano Energy 56 (2019) 33–39

Contents lists available at ScienceDirect

Nano Energy

journal homepage: www.elsevier.com/locate/nanoen

Full paper

Tribo-piezoelectricity in Janus transition metal dichalcogenide bilayers: A first-principles study

Haifang Cai[a], Yufeng Guo[a,b,*], Huajian Gao[b], Wanlin Guo[a]

[a] State Key Laboratory of Mechanics and Control of Mechanical Structures and MOE Key Laboratory for Intelligent Nano Materials and Devices, College of Aerospace Engineering, Nanjing University of Aeronautics and Astronautics, Nanjing 210016, China
[b] School of Engineering, Brown University, USA

ARTICLE INFO

Keywords:
Tribo-piezoelectricity
Janus TMD bilayer
First-principles calculations
Nanogenerator

ABSTRACT

Semiconducting Janus transition metal dichalcogenides (TMDs) are attractive for application in nanoscale electricity harvesting devices as their strong out-of-plane piezoelectricity. Here our extensive first-principles calculations reveal that in-plane interlayer sliding of Janus MXY (M = Mo or W, X/Y = S, Se, or Te, and X ≠ Y) bilayers would lead to significant enhancement of vertical piezoelectricity. The tribo-piezoelectric transduction mechanism is elucidated by tribological energy conversion of Janus TMD bilayers overcoming interlayer sliding resistance to reach the A-A stacking states that have the strongest out-of-plane piezoelectricity. Reducing interlayer distances of Janus TMD bilayers increases sliding energy barriers, and accordingly improves vertical charge polarization and inductive voltage generated between the top and bottom surfaces of Janus TMD bilayers. Based on the presented tribo-piezoelectricity, a compression-sliding design strategy is proposed for Janus TMD bilayers to create novel nanogenerators.

1. Introduction

Nanogenerators or energy harvesters that convert mechanical energy at nanoscale into electricity have attracted remarkable scientific interests and hold great promises for developing novel renewable energy generation technologies. Piezoelectric [1–3] and triboelectric [4–6] nanogenerators are now two major energy conversion techniques to harvest electricity. The former is based on the piezoelectric effect of semiconducting nanomaterials and nanostructures in which mechanical deformation or loading causes polarized charges [1], and the latter is based on the triboelectric effect in which electrostatic charges are generated at the interfaces of two materials by mechanical contact and friction [7]. Various semiconducting and ceramic nanomaterials such as ZnO and (1− x)Pb($Mg_{1/3}Nb_{2/3}$)O_3-$x$$PbTiO_3$ (PMN-PT) nanowires [8–11], lead zirconate titanate (PZT) and polyvinylidene fluoride (PVDF) nanofibers [12–14] as well as their composite structures with flexible substrates [15–17] have been used to fabricate piezoelectric nanogenerators. For triboelectric nanogenerators, there are usually two ways to generate electric polarization: vertical movement [18,19] or in-plane sliding [20,21] of two triboelectrically charged surfaces. On the other hand, through adding additional layers of ZnO nanorods or hybrid ZnO nanocomposites [22,23] into the interfaces between electrodes and their substrates, piezo-triboelectric nanogenerators with enhanced output current characteristics and energy conversion efficiency have been designed and fabricated. The corresponding working principle of those nanogenerators is to combine and integrate both the triboelectric and piezoelectric effects [22,23], where mechanical loading not only induces triboelectric charges at the ZnO layers and metal electrodes but also leads to piezoelectric polarization in the ZnO layers.

As typical two-dimensional (2D) materials, transition metal dichalcogenides (TMDs) are semiconducting and possess a wide range of application potentials in field-effect transistors [24,25], ultrathin photodetectors [25–27], and light-emitting devices [28,29]. In the field of energy harvesting, several experiments reported technical prototypes of 2D MoS_2 based piezoelectric nanogenerators that utilize the piezoelectricity and piezotronic effects of MoS_2 layers [30,31]. Moreover, 2D MoS_2 materials are also employed in triboelectric devices to achieve higher electricity output [32] and continuous direct-current [33] because of their flat surface and large contact area. Recently, Janus MoSSe monolayer in the 2 H phase has been successfully synthesized from original MoS_2 monolayers by chemical vapor deposition and thermal selenization methods with fully replacing the top-layer S by Se atoms [34,35]. The Janus configuration of MoSSe breaks the out-of-plane

* Corresponding author at: State Key Laboratory of Mechanics and Control of Mechanical Structures and MOE Key Laboratory for Intelligent Nano Materials and Devices, College of Aerospace Engineering, Nanjing University of Aeronautics and Astronautics, Nanjing 210016, China.
E-mail address: yfguo@nuaa.edu.cn (Y. Guo).

https://doi.org/10.1016/j.nanoen.2018.11.027
Received 29 September 2018; Received in revised form 12 November 2018; Accepted 12 November 2018
Available online 13 November 2018

structural symmetry and gives rise to a vertical dipole moment. Theoretical studies [36–38] further reveal that besides excellent in-plane piezoelectricity, Janus MXY (M = Mo or W, X/Y = S, Se, or Te, and X ≠ Y) monolayers and multilayers have stronger out-of-plane piezoelectric polarization than that of regular MoS_2 or $MoSe_2$ structures, which make them more suitable for nanoscale energy conversion device applications. However, the usage of Janus TMDs as major component in nanogenerators is seldom considered, and the feasibility and mechanism to generate electricity remain unclear.

In this study, we show by comprehensive first-principles calculations that transversely sliding two Janus TMD monolayers with each other along special direction could significantly strengthen the vertical charge polarization of the Janus TMD bilayer system. Such polarization enhancement is attributed to stronger out-of-plane piezoelectricity and interlayer charge redistribution when the Janus TMD bilayer overcomes in-plane sliding resistance and transforms into the A-A stacking state. Reducing interlayer distance of Janus TMD bilayer gives rise to larger in-plane sliding energy barrier and higher out-of-plane charge polarization. Different from previous piezo-triboelectric nanogenerators, we propose a strategy of compression-sliding to design electricity harvesting device based on the unveiled tribo-piezoelectricity in Janus TMD bilayers.

2. Model and method

First we consider a MoSSe bilayer. There are 2 Mo, 2 S and 2 Se atoms in the rhombus unit cell ($a_1 = a_2 = 3.234$ Å), respectively, and a vacuum region larger than 2.5 nm in the direction perpendicular to the plane. All computations are performed within the framework of density-functional theory (DFT) as implemented in the VASP code by using the projector augmented wave method with the Perdew-Burke-Ernzerhof (PBE) exchange-correlation functional [39–41]. The influence of vdW interactions is considered by using a modified version of vdW-DF, referred to as "optB86b-vdW," in which the PBE exchange functional of the original vdW-DF of Dion et al., is replaced with the optB86b exchange functional to yield more accurate equilibrium interatomic distances and energies for a wide range of systems [42,43]. The whole system is relaxed by using a conjugate-gradient algorithm until the force on each atom is less than 0.01 eV/nm. We find that the A-B and A-C stacking are two stable states, as shown in Fig. 1(a). The A-B stacking is chosen to be the initial state. Here the equilibrium interlayer distance d defined by the distance between surface Se and bottom S atoms is 0.96 nm for the A-B stacking. After structural relaxation, the top MoSSe monolayer is transversely sliding with respect to the bottom layer and translate relatively to different positions, and the whole system is relaxed again with the surface Se atoms of the top MoSSe monolayer and the bottom S atoms of the underlying monolayer being fixed to maintain constant interlayer distance. At different sliding positions, the computations with an energy cutoff of 500 eV and special k points sampled on a 15 × 15 × 1 Monkhorst-Pack mesh [44] are employed to calculate the total energy and vertical dipole moment D. The corresponding potential energy surfaces (PESs) for interlayer sliding are constructed by the difference between the energy and the lowest energy of the system. For the change in charge polarization during the process of sliding, we first calculate the vertical polarization P_d of the MoSSe bilayer with fixed interlayer distance by $P_d = D/A$, here A is the area of the MoSSe bilayer. Our DFT calculations show that charges will move to the interfacial S atoms as its stronger electronegativity when two Janus MoSSe monolayers are in contact at the initial equilibrium state, and the charge transfer leads to out-of-plane charge polarization. So we choose the vertical polarization $P_{F_n=0}$ of the MoSSe bilayer with the normal force F_n approximately relaxed to zero (see Fig. S1) as the reference point. Then the sliding polarization deviation surfaces (PDSs) of the MoSSe bilayers are constructed by $\Delta P = P_d - P_{F_n=0}$.

3. Results and discussion

Fig. 1(b) shows the PESs of in-plane interlayer sliding of MoSSe bilayers with interlayer distances of 0.96 and 0.93 nm. Obviously, the A-A stacking where the Mo, S and Se atoms in the top layer completely overlap with the same type of atoms in the bottom layer is the highest energy state. The maximum energy barrier for interlayer sliding increases with the interlayer distance decreases. From the corresponding PDSs shown in Fig. 1(c), it can be seen that vertical polarization of the MoSSe bilayer is significantly enhanced when the two Janus monolayers slide to the A-A stacking. Smaller interlayer distance leads to larger vertical polarization. The response of polarization change to interlayer distance in the A-B stacking is much weaker than that in the A-C stacking. So it is suitable to choose the A-B stacking as the initial state when considering to obtain the maximum polarization enhancement. Compared with the A-B stacking, the MoSSe bilayer with the A-A stacking has the highest out-of-plane piezoelectricity [36]. However, the A-A stacking is energetically unstable and cannot exist without external mechanical stimulation or constraint. In-plane sliding could trigger the transition of interlayer stacking of the MoSSe bilayer to the A-A stacking once the lateral driving force is beyond energy corrugation dependent interlayer shear strength and resistance force. Interlayer sliding and related resistance are tribological behaviors, while moving to the A-A stacking with fixed interlayer distance leads to remarkable strengthening of vertical polarization. Therefore, the in-plane interlayer sliding induced out-of-plane polarization enhancement can be considered as a tribo-piezoelectric effect in the MoSSe bilayer. The piezoelectricity comes from the tribological energy conversion that overcomes the energy barrier of sliding resistance. It should be mentioned that such tribo-piezoelectricity in MoSSe bilayer is different from conventional piezo-triboelectricity [22,23] as no triboelectric charges are generated by interlayer sliding.

The sliding energy corrugation ΔE in the PES of the MoSSe bilayer directly correlates with interlayer friction and resistance [45–47]. Higher maximum energy corrugation or barrier ΔE_{max} indicates stronger interlayer friction. Here the ΔE_{max} is defined by the energy corrugation between the initial A-B and A-A stacking states. As shown in Fig. 2(a), the maximum polarization deviation ΔP_{max} increases monotonically with the maximum energy barrier and the variation curve is approximately linear. To achieve larger vertical polarization needs more energy consumption on sliding friction. According to the maximum static resistance force f_{mr} acting on the MoSSe monolayer during the sliding process, the interlayer shear strength τ can be estimated by $\tau = |\frac{f_{mr}}{A}|$. The shear strength and maximum energy barrier quadratically increase as the interlayer distance decreases, as shown in Fig. 2(b). Those variations indicate that reducing interlayer distance of the MoSSe bilayer could be an effective way to add energy corrugation of in-plane interlayer sliding and accordingly enhance the conversion of tribological energy to electricity.

To further understand the tribo-piezoelectricity caused charge distribution in the MoSSe bilayer, in Fig. 3 we plot the charge density differences of the A-B and A-A stacking states with interlayer distances of 0.96 and 0.93 nm. The charge density difference is calculated by $\Delta\rho = \rho_{total} - \rho_{top} - \rho_{bottom}$, where ρ_{total} is the total charge density of the MoSSe bilayer, ρ_{top} and ρ_{bottom} are the charge densities of the top and bottom MoSSe monolayers, respectively. For the interlayer distance of 0.96 nm, charge accumulation in the A-B stacking state mainly locates around the S atoms of the top MoSSe monolayer and at the interface of the two monolayers. However, charge accumulation at the S atoms of the top layer is significantly enhanced after sliding to the A-A stacking state, and more charges transfer to the S atoms from the interface, as shown in Fig. 3(b). When the interlayer distance decreases to 0.93 nm, charge accumulation and depletion of the A-B and A-A stacking states are all improved, but the increasing magnitude of the A-A stacking is much higher than that of the A-B stacking. From the charge

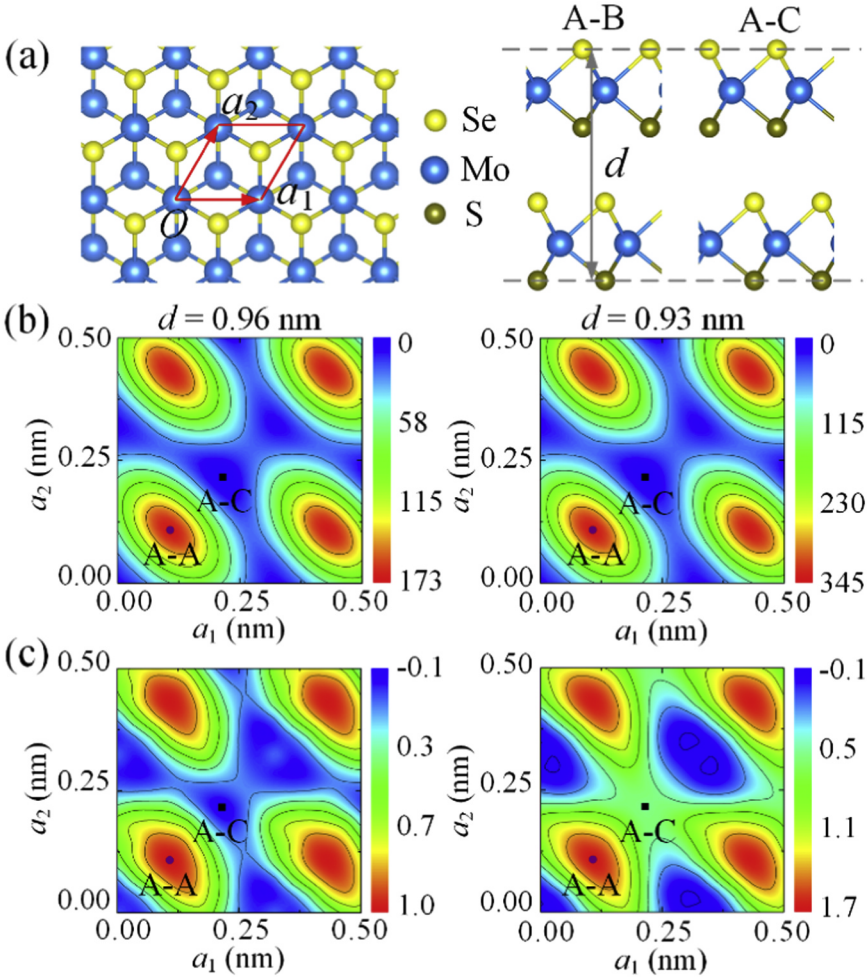

Fig. 1. The potential energy surfaces (PESs) and polarization deviation surfaces (PDSs) for interlayer sliding of MoSSe bilayer. (a) Top and side views of relaxed atomic configurations of an A-B stacking MoSSe bilayer, and side view of an A-C stacking bilayer. The lattice vectors a_1 and a_2 of the unit cell are marked by red lines, and d denotes the interlayer distance between surface Se and bottom S layers. (b) The PESs (in unit of meV) and (c) PDSs (in unit of pC/m) of the MoSSe bilayers when the top MoSSe layer slides with respect to the bottom layer for d = 0.96 nm and 0.93 nm, respectively. The dots in (b) and (c) donate the positions of the A-A and A-C stacking.

redistribution shown in Fig. 3, the stronger out-of-plane polarization of the A-A stacking MoSSe bilayer can be attributed to more charges concentrating on the interfacial S atoms.

Moreover, we calculate the average charge densities along the z direction of the A-B and A-A stacking MoSSe bilayers for different interlayer distances and zero normal force (see Fig. S2). Based on the average charge densities, the charge density differences $\Delta\rho^t$ and $\Delta\rho^b$ between the S and Se atoms belonging to the top and bottom MoSSe monolayers are calculated by

$$\Delta\rho^t = \Delta\rho_S^t - \Delta\rho_{Se}^t \text{ with } \Delta\rho_S^t = \rho_S^t - \rho_{S,\ F_n=0}^t \text{ and } \Delta\rho_{Se}^t = \rho_{Se}^t - \rho_{Se,\ F_n=0}^t ,$$

$$\Delta\rho^b = \Delta\rho_S^b - \Delta\rho_{Se}^b \text{ with } \Delta\rho_S^b = \rho_S^b - \rho_{S,\ F_n=0}^b \text{ and } \Delta\rho_{Se}^b = \rho_{Se}^b - \rho_{Se,\ F_n=0}^b .$$

Here ρ_S^t, ρ_{Se}^t, $\rho_{S,\ F_n=0}^t$, $\rho_{Se,\ F_n=0}^t$ and ρ_S^b, ρ_{Se}^b, $\rho_{S,\ F_n=0}^b$, $\rho_{Se,\ F_n=0}^b$ are the average z-direction charge densities of the S and Se atoms and the cases of zero normal force of the top and bottom MoSSe monolayers, respectively. For the A-B stacking, the charge density difference $\Delta\rho^t$ of the top monolayer increases as the interlayer distance is reduced while the $\Delta\rho^b$ of the bottom monolayer decreases, as shown in Fig. 4(a). On the contrary, the charge density differences $\Delta\rho^t$ and $\Delta\rho^b$ of the top and bottom monolayers for the A-A stacking sharply increases and remains approximately unchanged as the interlayer distance decreases (Fig. 4b), respectively. The different response of charge distribution between the A-B and A-A stacking states to the change in interlayer distance and the movement of electrons to the interfacial S atoms are consistent with the results shown in Fig. 3.

According to the unveiled tribo-piezoelectricity in MoSSe bilayer, we propose a strategy of compression-sliding to design nanogenerator. As shown in Fig. 4(c), a small amount of electrons move to the interfacial S and Se atoms at the initial A-B stacking state when the MoSSe bilayer is vertically compressed, but the number of electrons at the S atoms is higher than that at the Se atoms. Meanwhile, a small voltage with some inductive charges will be generated if there are two electrodes contacting with the top and bottom surfaces, as the MoSSe bilayer is semiconducting (see Fig. S3). Next, sliding the MoSSe bilayer to the A-A stacking with the same interlayer distance leads to more electrons concentrating around the interfacial S atoms. The top electrode thus will have more inductive charges. As a result, a larger voltage is created between the top and bottom electrode, as shown by Fig. 4(d). Such compression-sliding process in MoSSe bilayer provides a possible route to convert mechanical energy into electricity.

In order to obtain a quantitative estimation of the maximum generated voltage, the electrostatic potential differences ΔU between the Se atoms of the top layer and the S atoms of the bottom layer are calculated for the A-A stacking MoSSe bilayer. The difference ΔU is calculated by $\Delta U = \Delta U_{Se}^t - \Delta U_S^b$ with $\Delta U_{Se}^t = U_{Se}^t - U_{Se,F_{n=0}}^t$ and $\Delta U_S^b = U_S^b - U_{S,F_{n=0}}^b$, where U_{Se}^t, U_S^b, $U_{Se,F_n=0}^t$ and $U_{S,F_n=0}^t$ are the electrostatic potentials of the Se atoms of top layers, the S atoms of bottom layers and the corresponding cases of the zero normal forces, respectively (more details see Fig. S4). As shown in Fig. 5(a), the electrostatic potential difference of the A-A stacking state increases as the interlayer distance decreases. Furthermore, we estimate the voltages $\Delta\varphi$ induced between the top and bottom surfaces of the A-B and A-A stacking MoSSe bilayers in terms of $\Delta\varphi = \frac{\Delta U}{q}$, where q is the unit charge. In contrast to the slight change in the voltage of the A-B stacking state, the induced voltage of the A-A stacking increases with reduced interlayer distance (the inset of Fig. 5a) and the maximum voltage reaches to 0.25 V. Moreover, we consider other three high-symmetry stacking sequences

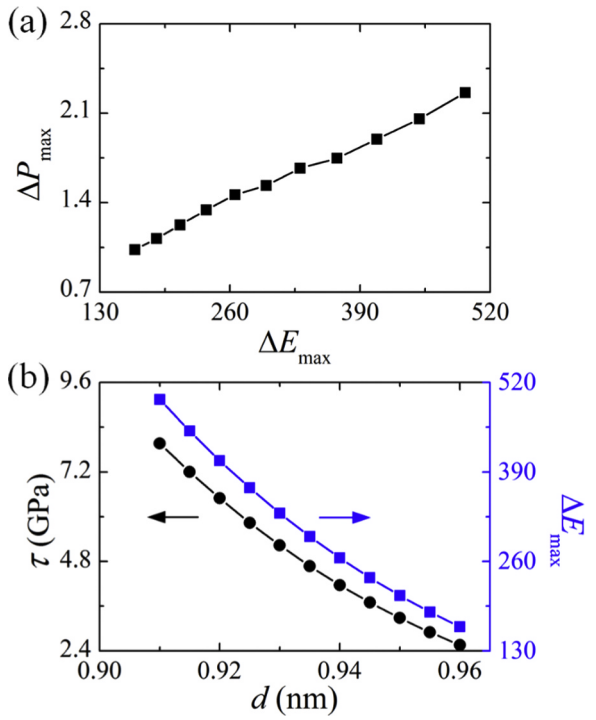

Fig. 2. Variations of (a) the maximum polarization deviations (in unit of pC/m) with the corresponding maximum sliding energy barriers (in unit of meV) when the interlayer distance decreases from 0.96 to 0.91 nm, and (b) the interlayer shear strength (black line with dots) and maximum sliding energy barriers (blue line with blocks) with the corresponding interlayer distance.

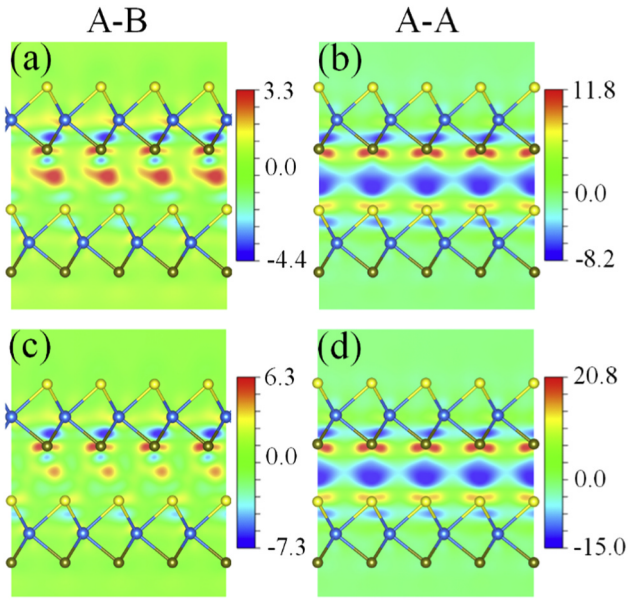

Fig. 3. 2D projections of charge density differences (in unit of 0.01 $e/Å^3$) of the A-B and A-A stacking MoSSe bilayers at d = 0.96 nm (a, b) and d = 0.93 nm (c, d). The atom denotation is the same as that in Fig. 1.

mentioned by the reference [36]. Similar to the A-B, A-A and A-C stacking states shown in Fig. 1, the Janus TMD bilayer can directly slide to the three sequences without rotation and the compression-sliding motions for these stacking sequences can also cause significant enhancement of vertical polarizations (see Fig. S5).

Besides the MoSSe bilayer, we also study the tribo-piezoelectricity in other Janus TMD bilayers by the same method and procedure. It can be seen from Fig. 5(b) that the maximum polarization deviations of all

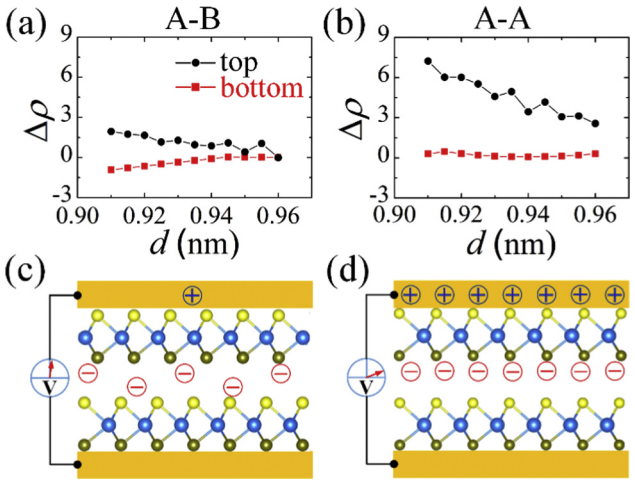

Fig. 4. (a, b) Variations of the average charge density differences (in unit of 0.001 $e/Å^3$) between the S and Se layers of the top and bottom MoSSe monolayers with interlayer distance for the (a) A-B stacking and (b) A-A stacking MoSSe bilayers. (c, d) Schematic illustrations of inductive charges and voltages generated at the electrodes that contact with the top and bottom surfaces of the (c) A-B stacking and (d) A-A stacking MoSSe bilayers with the same interlayer distance.

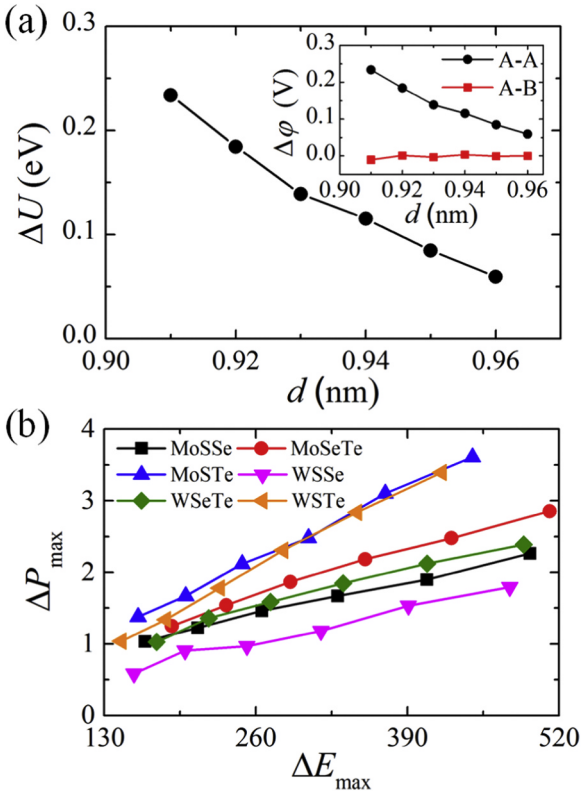

Fig. 5. (a) Variation of the electrostatic potential differences between the surface Se and bottom S layers with interlayer distances for the A-A stacking MoSSe bilayer. The inset shows the estimated voltages generated between the top and bottom surfaces of the A-B and A-A stacking MoSSe bilayers. (b) The maximum polarization deviations (in unit of pC/m) of various Janus TMD bilayers with the maximum sliding energy barriers (in unit of meV) at different interlayer distances.

Janus TMD bilayers monotonically increase with the sliding energy barriers. The enhancement of vertical polarization is observed to be strongest in MoSTe bilayer while that in WSSe bilayer is weakest. This difference indicates that the MoSTe bilayer will have the strongest

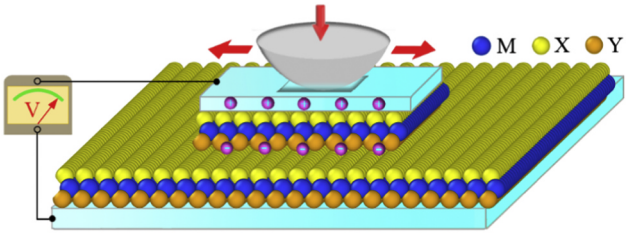

Fig. 6. Schematic diagram of working principle of the tribo-piezoelectricity in the Janus TMD bilayer, where the compression-sliding motion is manipulated by the probe or the movement of the underlying substrate. The probe and electrodes are denoted by gray and cyan colors, respectively.

tribo-piezoelectric effect when applying the compression-sliding motion.

The experimental feasibility of compression-sliding motion for the Janus TMD bilayers is of importance in practical application. Utilizing the nanoscale probe techniques, monolayer or few-layer of 2D materials have been successfully handled to slide or rotate along desired path and direction [48–52]. Normal load and pressure were applied on the planes of 2D materials through the vertical motion of the probe tip or the underlying work table [52,53], which could be used to reduce the interlayer distance of 2D materials. Based on the reported available technology, in Fig. 6 we present a possible schematic diagram of working principle of the Janus TMD bilayer for designing nanogenerator. Here a Janus TMD flake slides on a large monolayer Janus TMD substrate. The movement of the Janus TMD flake is driven by the attached electrode and probe, or by the motion of the underlying Janus TMD substrate. Meanwhile, the probe can also be used as a conductor to connect the bottom electrode [33]. Considering the commonly used Au electrode, further DFT calculations show that the adhesion between the Au electrode and Janus MoSSe monolayer is stronger than that between two Janus MoSSe monolayers, and the tribo-piezoelectricity of Janus MoSSe bilayer is slightly influenced by the Au contact (see Fig. S8 and S9 in Supplementary materials). Our theoretical and previous experimental results suggest that controllable interlayer sliding and modifying stacking state in Janus TMD bilayer as well as constructing the corresponding device are technically viable. Based on the energy conservation principle, the electric energy E_{elec} generated by the compression-sliding motion of the Janus TMD bilayer is mainly contributed by the tribology energy E_{tribo} that interlayer sliding consumes. So the electric energy E_{elec} can be approximately estimated by

$$E_{elec} = Pt \approx \delta E_{tribo},$$

where P is the power of the nanogenerator, t is the time, δ is the energy conversion coefficient as a part of tribology energy will transform into other type of energy such as thermal energy. In term of interlayer interactions between the Janus TMD layers and their periodic atomic structures (Fig. 1b), the interlayer sliding can be considered as stick-slip motion if the probe has a proper spring constant [54,55]. Assuming that the Janus TMD layer slides along a given direction, the tribology energy in one sliding period is deduced by $E_{tribo} = \frac{x\pi \Delta E_{max}}{2a}$ [54], where x is the displacement of the probe in one sliding period, a is the lattice periodicity of the Janus TMD layer, and ΔE_{max} is the maximum sliding energy barrier along this direction. According to the sliding velocity of the probe $v = x/t$, the power P of the nanogenerator in one sliding period can be approximately expressed as

$$P \approx \frac{v\pi\delta\Delta E_{max}}{2a}.$$

From the equation above, the power depends on the interlayer sliding energy barrier and the motion velocity of the probe. A larger normal pressure on the Janus TMD bilayer leads to a smaller interlayer distance and a higher ΔE_{max}. Therefore, the power of the Janus TMD nanogenerator could be effectively tuned by varying pressure and sliding velocity. Furthermore, the power density (the power per unit area) in one sliding period is estimated by using the sliding velocities from 1 to 100 nm/s and the ΔE_{max} of the case that the interlayer distance is compressed to 0.93 nm. The sliding velocities from 1 to 100 nm/s are available and commonly used for the probe tips in the practical situation. Assuming that the tribological energy completely transfers into electric energy, the power densities generated by the tribo-piezoelectricity are estimated to be from 296.39 to 29,639 $\mu W\,cm^{-2}$ when the probe velocities vary from 1 to 100 nm/s. For comparison, the reported power density of the piezo-triboelectric nanogenerator in experimental test is 7 μWcm^{-2} [22]. In previous studies, the power densities of the piezoelectric nanogenerators (PENGs) are from 4.41 to 5.92 $\mu W\,cm^{-2}$ [56,57], and for the triboelectric nanogenerators (TENGs) the power densities are reported from 400 to 50000 μWcm^{-2} [58–62]. Obviously, the ideal power densities generated by the compression-sliding motion of the Janus TMD bilayers are much higher than that of most reported nanogenerators, and can also be comparable to the high power densities generated in some TENGs by modifying the sliding velocity.

4. Conclusion

In summary, in-plane moving two Janus TMD monolayers with fixed interlayer distance could give rise to significant enhancement of out-of-plane piezoelectricity. The tribo-piezoelectric effect originates from tribological energy conversion of sliding Janus TMD bilayer from the initial A-B to the A-A stacking state that possesses the largest out-of-plane piezoelectricity, and no triboelectric charges are created during the process of interlayer motion. According to the tribo-piezoelectricity revealed in Janus TMD bilayers, a strategy of compression-sliding is proposed to create nanogenerators with high power densities. Our results provide some new insights into the application of Janus TMD materials in energy conversion and harvesting devices.

Acknowledgements

This work is supported by the National Science Foundation of China (11472131, 51535005 and 11622218), the Program for New Century Excellent Talents in University, China (NCET-13-0855), the National Science Foundation of Jiangsu Province, China (BK20160037), the Fundamental Research Funds for the Central Universities of China (NJ20150048 and INMD-2015M02), and the Research Fund of State Key Laboratory of Mechanics and Control of Mechanical Structures, China (Nanjing University of Aeronautics and Astronautics) (MCMS 0414G01 and 0416K01), a Project Funded by the Priority Academic Program Development of Jiangsu Higher Education Institutions, China. Postgraduate Research & Practice Innovation Program of Jiangsu Province, China (KYCX17_0229).

Competing interests

The authors declare no competing financial interests.

Appendix A. Supplementary material

Supplementary data associated with this article can be found in the online version at doi:10.1016/j.nanoen.2018.11.027.

References

[1] Z.L. Wang, J.H. Song, Piezoelectric nanogenerators based on zinc oxide nanowire arrays, Science 312 (2006) 242–246.
[2] S. Xu, Y. Qin, C. Xu, Y. Wei, R. Yang, Z.L. Wang, Self-powered nanowire devices, Nat. Nanotechnol. 5 (2010) 366–373.

[3] G. Zhu, R. Yang, S. Wang, Z.L. Wang, Flexible high-output nanogenerator based on lateral ZnO nanowire array, Nano Lett. 10 (2010) 3151–3155.
[4] F.R. Fan, L. Lin, G. Zhu, W. Wu, R. Zhang, Z.L. Wang, Transparent Triboelectric nanogenerators and self-powered pressure sensors nased on micropatterned plastic films, Nano Lett. 12 (2012) 3109–3114.
[5] F.R. Fan, Z.Q. Tian, Z.L. Wang, Flexible triboelectric generator, Nano Energy 1 (2012) 328–334.
[6] Z.L. Wang, Triboelectric nanogenerators as new energy technology for self-powered systems and as active mechanical and chemical sensors, ACS Nano 7 (2013) 9533–9557.
[7] G. Zhu, B. Peng, J. Chen, Q. Jing, Z.L. Wang, Triboelectric nanogenerators as a new energy technology: from fundamentals, devices, to applications, Nano Energy 14 (2015) 126–138.
[8] Y. Gao, Z.L. Wang, Electrostatic potential in a bent piezoelectric nanowire. The fundamental theory of nanogenerator and nanopiezotronics, Nano Lett. 7 (2007) 2499–2505.
[9] M.P. Lu, J. Song, M.Y. Lu, M.T. Chen, Y. Gao, L.J. Chen, Z.L. Wang, Piezoelectric nanogenerator using p-type ZnO nanowire arrays, Nano Lett. 9 (2009) 1223–1227.
[10] S. Xu, G. Poirier, N. Yao, PMN-PT nanowires with a very high piezoelectric constant, Nano Lett. 12 (2012) 2238–2242.
[11] S. Xu, Y.W. Yeh, G. Poirier, M.C. McAlpine, R.A. Register, N. Yao, Flexible piezoelectric PMN-PT nanowire-based nanocomposite and device, Nano Lett. 13 (2013) 2393–2398.
[12] J. Chang, M. Domnner, C. Chang, L. Lin, Piezoelectric nanofibers for energy scavenging applications, Nano Energy 1 (2012) 356–371.
[13] X. Chen, S. Xu, N. Yao, Y. Shi, 1.6 V nanogenerator for mechanical energy harvesting using PZT nanofibers, Nano Lett. 10 (2010) 2133–2137.
[14] C. Chang, V.H. Tran, J. Wang, Y.K. Fuh, L. Lin, Direct-write piezoelectric polymeric nanogenerator with high energy conversion efficiency, Nano Lett. 10 (2010) 726–731.
[15] I.J. No, D.Y. Jeong, S. Lee, S.H. Kim, J.W. Cho, P.K. Shin, Enhanced charge generation of the ZnO nanowires/PZT hetero-junction based nanogenerator, Microelectron. Eng. 110 (2013) 282–287.
[16] M. Lee, C.Y. Chen, S. Wang, S.N. Cha, Y.J. Park, J.M. Kim, L.J. Chou, Z.L. Wang, A hybrid piezoelectric structure for wearable nanogenerators, Adv. Mater. 24 (2012) 1759–1764.
[17] G. Wang, Y. Deng, Y. Xiang, L. Guo, Fabrication of radial ZnO nanowire clusters and radial ZnO/PVDF composites with enhanced dielectric properties, Adv. Funct. Mat. 18 (2008) 2584–2592.
[18] G. Zhu, C.F. Pan, W.X. Guo, C.Y. Chen, Y.S. Zhou, R.M. Yu, Z.L. Wang, Triboelectric-generator-driven pulse electrodeposition for micropatterning, Nano Lett. 12 (2012) 4960–4965.
[19] S. Wang, L. Lin, Z.L. Wang, Nanoscale Triboelectric-effect-enabled energy conversion for sustainably powering portable electronics, Nano Lett. 12 (2012) 6339–6346.
[20] S. Wang, L. Lin, Y. Xie, Q. Jing, S. Niu, Z.L. Wang, Sliding-triboelectric nanogenerators based on in-plane charge-separation mechanism, Nano Lett. 13 (2013) 2226–2233.
[21] G. Zhu, J. Chen, Y. Liu, P. Bai, Y.S. Zhou, Q. Jing, C. Pan, Z.L. Wang, Linear-grating triboelectric generator based on sliding electrification, Nano Lett. 13 (2013) 2282–2289.
[22] X. Yang, W.A. Daoud, Triboelectric and piezoelectric effects in a combined tribo-piezoelectric nanogenerator based on an interfacial ZnO nanostructure, Adv. Funct. Mater. 26 (2016) 8194–8201.
[23] S.C. Karumuthil, S.P. Rajeev, S. Varghese, Piezo-tribo nanoenergy harvester using hybrid polydimethyl siloxane based nanocomposite, Nano Energy 40 (2017) 487–494.
[24] B. Radisavljevic, A. Radenovic, J. Brivio, V. Giacometti, A. Kis, Single-layer MoS_2 transistors, Nat. Nanotechnol. 6 (2011) 147–150.
[25] Q.H. Wang, K. Kalantar-Zadeh, A. Kis, J.N. Coleman, M.S. Strano, Electronics and optoelectronics of two-dimensional transition metal dichalcogenides, Nat. Nanotechnol. 7 (2012) 699–712.
[26] D. Jariwala, V.K. Sangwan, L.J. Lauhon, T.J. Marks, M.C. Hersam, Emerging device applications for semiconducting two-dimensional transition metal dichalcogenides, ACS Nano 8 (2014) 1102–1120.
[27] D. Lopez-Sanchez, M. Lembke, A. Kayci, A. Radenovic, Kis, Ultrasensitive photodetectors based on monolayer MoS_2, Nat. Nanotechnol. 8 (2013) 497–501.
[28] P. Rivera, J.R. Schaibley, A.M. Jones, J.S. Ross, S. Wu, G. Aivazian, P. Klement, K. Seyler, G. Clark, N.J. Ghimire, J. Yan, D.G. Mandrus, W. Yao, X. Xu, Observation of long-lived interlayer excitons in monolayer $MoSe_2$-WSe_2 heterostructures, Nat. Commun. 6 (2015) 6242.
[29] J.S. Ross, P. Klement, A.M. Jones, N.J. Ghimire, J. Yan, D.G. Mandrus, T. Taniguchi, K. Watanabe, K. Kitamura, W. Yao, D.H. Cobden, X. Xu, Electrically tunable excitonic light-emitting diodes based on monolayer WSe_2 p-n junctions, Nat. Nanotechnol. 9 (2014) 268–272.
[30] W. Wu, L. Wang, Y. Li, F. Zhang, L. Lin, S. Niu, D. Chenet, X. Zhang, Y. Hao, T.F. Heinz, J. Hone, Z.L. Wang, Piezoelectricity of single-atomic-layer MoS_2 for energy conversion and piezotronics, Nature 514 (2014) 470.
[31] K. Maity, B. Mahanty, T.K. Sinha, S. Garain, A. Biswas, S.K. Ghosh, S. Manna, S.K. Ray, D. Mandal, Two-dimensional piezoelectric MoS_2-modulated nanogenerator and nanosensor made of poly(vinlydine fluoride) nanofiber webs for self-powered electronics and robotics, Energy Technol. 5 (2017) 234–243.
[32] C. Wu, T.W. Kim, J.H. Park, H. An, J. Shao, X. Chen, Z.L. Wang, Enhanced triboelectric nanogenerators based on MoS_2 monolayer nanocomposites acting as electron-acceptor layers, ACS Nano 11 (2017) 8356–8363.
[33] J. Liu, A. Goswami, K. Jiang, F. Khan, S. Kim, R. McGee, Z. Li, Z. Hu, J. Lee, T. Thundat, Direct-current triboelectricity generation by a sliding Schottky nanocontact on MoS_2 multilayers, Nat. Nanotechnol. 13 (2018) 112–116.
[34] A.Y. Lu, H. Zhu, J. Xiao, C.P. Chu, Y. Han, M.H. Chiu, C.C. Cheng, C.W. Yang, K.H. Wei, Y. Yang, Y. Wang, D. Sokaras, D. Nordlund, P. Yang, D.A. Muller, M.Y. Chou, X. Zhang, L.J. Li, Janus monolayers of transition metal dichalcogenides, Nat. Nanotechnol. 12 (2017) 744.
[35] J. Zhang, S. Jia, I. Kholmanov, L. Dong, D. Er, W. Chen, H. Guo, Z. Jin, V.B. Shenoy, L. Shi, J. Lou, Janus monolayer transition-metal dichalcogenides, ACS Nano 11 (2017) 8192–8198.
[36] L. Dong, J. Lou, V.B. Shenoy, Large in-plane and vertical piezoelectricity in Janus transition metal dichalchogenides, ACS Nano 11 (2017) 8242–8248.
[37] F. Li, W. Wei, P. Zhao, B. Huang, Y. Dai, Electronic and optical properties of pristine and vertical and lateral heterostructures of Janus MoSSe and WSSe, J. Phys. Chem. Lett. 8 (2017) 5959–5965.
[38] W.J. Yin, B. Wen, G.Z. Nie, X.L. Wei, L.M. Liu, Tunable dipole and carrier mobility for a few layer Janus MoSSe structure, J. Mater. Chem. C 6 (2018) 1693–1700.
[39] J.P. Perdew, K. Burke, M. Ernzerhof, Generalized gradient approximation made simple, Phys. Rev. Lett. 77 (1996) 3865.
[40] G. Kresse, J. Furthmüller, Efficient iterative schemes for ab initio total-energy calculations using a plane-wave basis set, Phys. Rev. B 54 (1996) 11169.
[41] P.E. Blöchl, Projector augmented-wave method, Phys. Rev. B 50 (1994) 17953.
[42] J. Klimeš, D.R. Bowler, A. Michaelides, Chemical accuracy for the van der Waals density functional, J. Phys. Condens. Mat. 22 (2009) 022201.
[43] J. Klimeš, D.R. Bowler, A. Michaelides, Van der Waals density functionals applied to solids, Phys. Rev. B 83 (2011) 195131.
[44] H.J. Monkhorst, J.D. Pack, Special points for Brillouin-zone integrations, Phys. Rev. B 13 (1976) 5188.
[45] Y. Guo, J. Qiu, W. Guo, Reduction of interfacial friction in commensurate graphene/h-BN heterostructures by surface functionalization, Nanoscale 8 (2016) 575–580.
[46] S.N. Medyanik, W.K. Liu, I.H. Sung, R.W. Carpick, Predictions and observations of multiple slip modes in atomic-scale friction, Phys. Rev. Lett. 97 (2006) 136106.
[47] E. Riedo, E. Gnecco, R. Bennewitz, E. Meyer, H. Brune, Interaction potential and hopping dynamics governing sliding friction, Phys. Rev. Lett. 91 (2003) 084502.
[48] Y. Song, D. Mandelli, O. Hod, M. Urbakh, M. Ma, Q. Zheng, Robust microscale superlubricity in graphite/hexagonal boron nitride layered heterojunctions, Nat. Mater. 17 (2018) 894–899.
[49] S.W. Liu, H.P. Wang, Q. Xu, T.B. Ma, G. Yu, C. Zhang, D. Geng, Z. Yu, S. Zhang, W. Wang, Y.Z. Hu, H. Wang, J. Luo, Robust microscale superlubricity under high contact pressure enabled by graphene-coated microsphere, Nat. Commun. 8 (2017) 14029.
[50] H. Li, J. Wang, S. Gao, Q. Chen, L. Peng, K. Liu, X. Wei, Superlubricity between MoS_2 monolayers, Adv. Mater. 29 (2017) 1701474.
[51] P.E. Sheehan, C.M. Lieber, Friction between van der Waals solids during lattice directed sliding, Nano Lett. 17 (2017) 4116–4121.
[52] C.C. Vu, S. Zhang, M. Urbakh, Q. Li, Q.C. He, Q. Zheng, Observation of normal-force-independent superlubricity in mesoscopic graphite contacts, Phys. Rev. B 94 (2016) 081405.
[53] M. Dienwiebel, G.S. Verhoeven, N. Pradeep, J.W.M. Frenken, J.A. Heimberg, H.W. Zandbergen, Superlubricity of graphite, Phys. Rev. Lett. 92 (2004) 126101.
[54] A. Socoliuc, R. Bennewitz, E. Gnecco, E. Meyer, Transition from stick-slip to continuous sliding in atomic friction: entering a new regime of ultralow friction, Phys. Rev. Lett. 92 (2004) 134301.
[55] S.N. Medyanik, W.K. Liu, I.H. Sung, R.W. Carpick, Predictions and observations of multiple slip modes in atomic-scale friction, Phys. Rev. Lett. 97 (2006) 136106.
[56] V. Bhavanasi, V. Kumar, K. Parida, J. Wang, P.S. Lee, Enhanced piezoelectric energy harvesting performance of flexible PVDF-TrFE bilayer films with graphene oxide, ACS Appl. Mater. Interfaces 8 (2016) 521–529.
[57] W. Jin, Z. Wang, H. Huang, X. Hu, Y. He, M. Li, L. Li, Y. Gao, Y. Hu, H. Gu, High-performance piezoelectric energy harvesting of vertically aligned $Pb(Zr,Ti)O_3$ nanorod arrays, RSC Adv. 8 (2018) 7422–7427.
[58] J.W. Lee, H.J. Cho, J. Chun, K.N. Kim, S. Kim, C.W. Ahn, I.W. Kim, J.Y. Kim, S.W. Kim, C. Yang, J.M. Baik, Robust nanogenerators based on graft copolymers via control of dielectrics for remarkable output power enhancement, Sci. Adv. 3 (2017) e1602902.
[59] W. Yang, J. Chen, G. Zhu, J. Yang, P. Bai, Y. Su, Q. Jing, X. Cao, Z.L. Wang, Harvesting energy from the natural vibration of human walking, ACS Nano 7 (2013) 11317–11324.
[60] S. Wang, Y. Xie, S. Niu, L. Lin, C. Liu, Y.S. Zhou, Z.L. Wang, Maximum surface charge density for triboelectric nanogenerators achieved by ionized-air injection: methodology and theoretical understanding, Adv. Mater. 26 (2014) 6720–6728.
[61] W. Tang, T. Jiang, F.R. Fan, A.F. Yu, C. Zhang, X. Cao, Z.L. Wang, Liquid-metal electrode for high-performance triboelectric nanogenerator at an instantaneous energy conversion efficiency of 70.6%, Adv. Funct. Mater. 25 (2015) 3718–3725.
[62] G. Zhu, Y.S. Zhou, P. Bai, X.S. Meng, Q. Jing, J. Chen, Z.L. Wang, A shape-adaptive thin-film-based approach for 50% high-efficiency energy generation through micro-grating sliding electrification, Adv. Mater. 26 (2014) 3788–3796.

Haifang Cai is a Ph.D. candidate in College of Aerospace Engineering, Nanjing University of Aeronautics and Astronautics under the supervision of Prof. Yufeng Guo. His research interests include the coupled mechanical, electronic properties of low-dimensional materials and their applications in the field of energy conversion.

Yufeng Guo is a Professor in College of Aerospace Engineering, Nanjing University of Aeronautics and Astronautics. Dr. Guo received his Ph.D. degree in solid mechanics from Nanjing University of Aeronautics and Astronautics in 2006. His research focuses on multi-field coupling mechanism, properties and design of nanoscale functional devices and systems utilizing first-principles calculations, molecular dynamics simulations and mechanics modeling.

Huajian Gao received his B.S. degree from Xi'an Jiaotong University of China in 1982, and his M.S. and Ph.D. degrees in Engineering Science from Harvard University in 1984 and 1988, respectively. At present, he is the Walter H. Annenberg Professor of Engineering at Brown University. His researches focus on the understanding of basic principles that control mechanical properties and behaviors of materials in both engineering and biological systems.

Wanlin Guo received his Ph.D. from Northwestern Polytechnical University in solid mechanics. He is currently a full time professor and director in Institute of Nanoscience, Key Laboratory of Intelligent Nano Mechanics and Control for Mechanical Structures. Deputy director of State Key Laboratory of Mechanics and Control of Mechanical Structures in Nanjing University of Aeronautics and Astronautics. His researches focus on nanoscale physical mechanics, intelligent nanomaterials and devices, highly efficient energy transfer nanotechnology, three-dimensional fatigue fracture and damage tolerance and durability design of structures.